Journal of Materials Chemistry C

ROYAL SOCIETY OF CHEMISTRY

PAPER

View Article Online
View Journal | View Issue

Cite this: J. Mater. Chem. C, 2023, 11, 4033

Design of high-performance circularly polarized multiple resonance-based TADF materials *via* participatory chiral perturbation†

Ping Li, Wenjing Li, Qixin Lv, Runfeng Chen * and Chao Zheng*

Multiple-resonance thermally activated delayed fluorescence (MR-TADF) materials have attracted tremendous attention recently, but it remains a formidable challenge to design circularly polarized MR-TADF (CP-MR-TADF) emitters concurrently exhibiting high quantum efficiency, narrowband emission and high dissymmetry factor. Here, we perform a systematic theoretical investigation on the design of high-performance CP-MR-TADF materials *via* participatory chiral perturbation by regulating the introduction modes of peripheral groups and types of electron-donating chiral perturbation units capable of directly participating in the TADF emission. The designed molecules maintain the multiple-resonance characteristics with narrowband emissions after the introduction of chiral units. And, the *meta*-PhCN-based and PhCN-free molecules with the moderate electron-donating chiral unit of BAM exhibit excellent performance in light of the narrowband emissions, large dissymmetry factors, facile reverse intersystem crossing channels with large spin–orbit coupling values and efficient fluorescence radiative rates. It was found that the small centroid distance between the chiral unit and the multiple-resonance B/N skeleton, and the obvious chiral unit participation in the frontier molecular orbital distributions should be two key factors in realizing a large degree of chiral perturbation of the circularly polarized luminescent (CPL) signals of materials. These findings and insights are important as they reveal the structure–property relationship of CP-MR-TADF materials constructed using a chiral perturbation strategy, providing an in-depth understanding of the design of such high-performance materials.

Received 8th December 2022,
Accepted 19th February 2023

DOI: 10.1039/d2tc05229f

rsc.li/materials-c

1. Introduction

Circularly polarized organic light-emitting diodes (CP-OLEDs) have received widespread attention in recent years owing to their promising applications in 3D displays.[1–4] As a crucial component of CP-OLEDs, organic chiral emitters play a dominant role in determining the device performance. Great efforts have been made to construct efficient emitters with desirable circularly polarized luminescence (CPL) properties of high quantum efficiency, excellent color purity, and large dissymmetry factor (g).[5–11] The traditional circularly polarized thermally activated delayed fluorescence (CP-TADF) materials synthesized with donor–acceptor (D–A) architectures showed promising quantum efficiency due to their nearly 100% internal quantum efficiency in harvesting both singlet and triplet excitons, but suffered from broad emission spectra because of the remarkable vibronic coupling between the ground state (S_0) and the lowest singlet excited state (S_1) as well as the significant structure relaxation of the S_1 state. Recently, multiple resonance TADF (MR-TADF) emitters have become popular luminescent materials with narrowband emissions achieved by integrating the opposite resonance effects of electron-deficient boron atoms and electron-donating nitrogen/oxygen atoms in one rigid aromatic framework to inhibit the molecular relaxations and weaken the vibronic couplings.[12–19] Developing MR-TADF skeletons with circularly polarized luminescence properties is a new design strategy to develop high performance circularly polarized MR-TADF (CP-MR-TADF) materials simultaneously exhibiting high quantum efficiency, narrowband emission and circularly polarized luminescence.

To date, several CP-MR-TADF materials with high quantum efficiency, narrowband emissions and circularly polarized electroluminescence spectral features have been developed and used in CP-OLEDs. For instance, Li *et al.*[20] developed two pairs of chiral MR-TADF emitters by grafting chiral *R*/*S*-octahydrobinaphthol (*R*/*S*-OBN) units onto a typical MR-core *via* a chiral perturbation strategy, achieving a maximum external quantum efficiency (EQE_{max}) of 29.4% and an

State Key Laboratory of Organic Electronics and Information Displays & Jiangsu Key Laboratory for Biosensors, Institute of Advanced Materials (IAM), Nanjing University of Posts & Telecommunications, 9 Wenyuan Road, Nanjing, 210023, China. E-mail: iamrfchen@njupt.edu.cn

† Electronic supplementary information (ESI) available. See DOI: https://doi.org/10.1039/d2tc05229f

electroluminescence dissymmetry factor (g_{EL}) on the order of 10^{-4}; this is the first example of CP-OLEDs that exhibited clear circularly polarized electroluminescence (CPEL) signals, narrow emission bands and TADF properties. Apart from axial chirality, Wu *et al.*[21] designed helical boron/nitrogen (B/N)-based enantiomers with asymmetrical peripheral-lock; the fabricated OLEDs achieved an EQE_{max} of 26.5%/20.6%, a narrow full width at half maximum (FWHM) of 48/49 nm, and a g_{EL} on the order of 10^{-3}. The excellent circularly polarized emission results from their helical molecular structures participating in the low-lying electronic transition. Other B/N and carbonyl/nitrogen (C=O/N) type MR-TADF materials also showed unambiguous CPEL signals by adopting the intrinsic helical chirality within the hetero-helicene structures.[22–25] In another study reported by Yang *et al.*,[26] a pair of chiral emitters was designed by integrating molecular rigidity, central chirality and the MR effect. The enantiomer-based CP-OLEDs achieved an outstanding EQE_{max} of 37.2%/36.1%, a narrow FWHM of 30/30 nm, and distinct CPEL signals with a g_{EL} on the order of 10^{-4}. Besides, Liao *et al.*[27] designed two efficient chiral emitters by introducing the planar chirality into the typical B/N MR system, of which the first nearly pure green-emitter-based device exhibited an excellent EQE_{max} of 28.7%, a FWHM of 36 nm, and a g_{EL} on the order of 10^{-3}. Compared with the helical materials requiring relatively complicated molecular design and multiple synthesis steps, the CP-MR-TADF materials can be designed using a chiral perturbation strategy with commercial chiral enantiomer products as the initial raw materials, which significantly promotes the large-scale molecular synthesis and flexible molecular design.[28–33] However, the materials designed with the chiral perturbation strategy show relatively low g_{EL} values mainly due to the non-participating chiral perturbation and the lack of molecular design guidelines. Therefore, an in-depth understanding of the molecular structure–performance relationship is of high importance and an updated molecular design strategy of high-performance CP-MR-TADF materials *via* chiral perturbation is in high demand.

Here, we propose a participatory chiral perturbation strategy to enable the direct participation of chiral units in emission by regulating the introduction modes of peripheral segments and types of electron-donating chiral units (Fig. 1). With the classical B/N multiple resonance skeleton (BN) as the MR core, the chiral units were directly connected onto the BN molecular skeleton, or linked to the electron-withdrawing phenyl-cyanide (PhCN) group, where PhCN was introduced onto the *para*- or *meta*-carbon position of the B-substituted phenyl ring of BN, to obtain molecules with different introduction modes of peripheral segments. Furthermore, five common chiral units of octahydrobinaphthol (OBN), binaphthol (BNA), diphenylbinaphthalamine (BAM), diaminocyclohexane (CAI) and diphenyldiaminocyclohexane (PhCAI) with gradually enhanced electron-donating abilities (Fig. S1, ESI†) were chosen to adjust the CPL signals. It was found that the molecules with the chiral units directly connecting onto the BN molecular skeleton (PhCN-free molecules) and the *meta*-PhCN-based molecules possessed relatively favorable g_{EL} properties, indicating that the small centroid distance between the chiral unit and the B/N skeleton, and the participation of chiral perturbation units in the frontier molecular orbital distributions are efficient in realizing a large degree of chiral perturbation. Moreover, the molecules with a moderate electron-donating chiral unit of BAM would be promising high-performance CP-MR-TADF materials owing to their excellent balance between the contradictory requirements of a large g value and high fluorescence quantum yield. These theoretical calculations would give important photophysical insights on the structure–property relationship and provide new guidelines to construct high-performance CP-MR-TADF materials *via* an updated chiral perturbation strategy.

2. Computational details

Ground-state and excited-state geometry optimizations, and related property calculations were performed using density functional theory (DFT) and time-dependent DFT (TD-DFT) methods, respectively. For the TADF molecules featuring intramolecular charge transfer excitations, DFT/TD-DFT methods with the inclusion of a fixed percentage of nonlocal Hartree–Fock exchange (HF_{exc}) in the functional are commonly employed to predict their ground-state and excited-state properties. Herein, the hybrid functional of B3LYP (20% HF_{exc}) and the basis set of 6-31G(d,p), which have been widely used for the property simulations of MR materials,[14,34–41] were selected to optimize the ground-state and excited state geometries and carry out the related property calculations. Frequency calculations were carried out at the same level to confirm that the optimized geometries are stable structures. To further verify the accurate description of excited-state properties, TD-DFT methods with hybrid functionals of O3LYP (11.6% HF_{exc}), B3LYP, and PBE0 (25% HF_{exc}) and a range-separated functional CAM-B3LYP (19% HF_{exc} at short-range and 65% HF_{exc} at long-range) were chosen to simulate the absorption spectrum of the experimental molecule *p*-BN-OBN in toluene by using the polarized continuum model (PCM).[42] The calculated results indicate that the B3LYP method indeed provides relatively accurate the maximum absorption wavelength compared to the experimental data (see Table S1, ESI†). All the calculations were carried out using the Gaussian 09 software package. The analyses of the centroid distance between molecular fragments were done using Multiwfn software,[43] the spin–orbit coupling (SOC) matrix elements between singlet and triplet states were calculated with the ORCA 5.0.1 version,[44] and the reorganization energy (λ) and the fluorescence radiative rate were calculated using the Molecular Materials Property Prediction Package (MOMAP) with the Electron Vibration Coupling (EVC) module.[45,46]

3. Results and discussion

3.1 Geometric structure–property analyses

The optimized S_0 and S_1 geometries of the designed molecules were investigated. The geometrical structures of OBN series molecules in the S_0 state as examples are shown in Fig. 1, and the structural parameters as indicated in Fig. 1 of all the

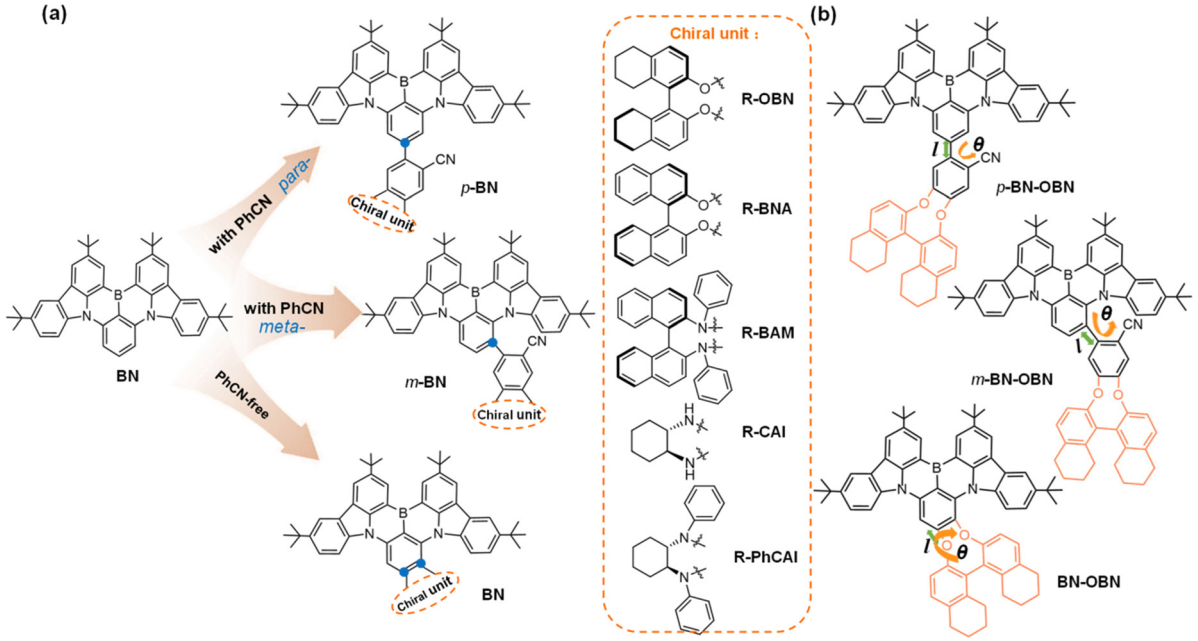

Fig. 1 (a) Design of high-performance CP-MR-TADF materials by regulating the introduction modes of peripheral groups and types of chiral units. (b) Structures of the experimental molecule of *p*-BN-OBN and the representative molecules.

molecules are collected in Table 1. Compared with the *para*-PhCN- and *meta*-PhCN-based molecules, the PhCN-free molecules have smaller bond length (l) values due to the intrinsic bond type difference (C–C *vs.* C–O/N), of which BN-BAM and BN-PhCAI exhibit relatively larger l values mainly because of the steric hindrance of phenyl groups. There is basically little difference in l values (0–0.03 Å) between S_0 and S_1 states for the studied molecules, yet the interested dihedral angles (θ) show complex changes upon excitation, which originates from the geometrical steric hindrance effect and electronic interactions between adjacent groups. For the molecules with chiral units of OBN, BN and BAM, the *para*-PhCN-, *meta*-PhCN-based and PhCN-free molecules present gradually decreased $\Delta\theta$ values between S_0 and S_1 states, indicating the possible increased electron communications between the MR core and chiral perturbation units. For the CAI- and PhCAI-based molecules, the stronger electron-donating chiral units should make nonnegligible influences on the optoelectronic properties in spite of the irregular changing $\Delta\theta$ values, which will be discussed below.

Table 1 Calculated bond lengths, dihedral angles (as indicated in Fig. 1) and RMSDs of the investigated molecules

	l (Å)		θ (°)		$\Delta\theta$ (°)	RMSD
Compd.	S_0	S_1	S_0	S_1	$\lvert S_1–S_0\rvert$	S_1/S_0
p-BN-OBN	1.49	1.46	46.2	34.5	11.7	0.38
m-BN-OBN	1.49	1.48	48.9	43.4	5.5	0.16
BN-OBN	1.38	1.38	46.8	49.2	2.4	0.25
p-BN-BNA	1.49	1.46	49.2	34.0	15.2	0.37
m-BN-BNA	1.49	1.48	50.2	45.8	4.4	0.23
BN-BNA	1.38	1.38	46.0	49.7	3.7	0.25
p-BN-BAM	1.49	1.46	43.0	33.0	10.0	0.46
m-BN-BAM	1.49	1.47	51.3	43.6	7.7	0.25
BN-BAM	1.42	1.42	53.1	55.2	2.1	0.27
p-BN-CAI	1.49	1.48	46.2	41.6	4.6	0.12
m-BN-CAI	1.49	1.46	50.9	41.3	9.6	0.28
BN-CAI	1.38	1.39	9.0	19.2	10.2	0.25
p-BN-PhCAI	1.49	1.48	45.5	43.3	2.2	0.09
m-BN-PhCAI	1.49	1.47	50.5	41.7	8.8	0.33
BN-PhCAI	1.40	1.40	25.1	22.9	2.2	0.21

To quantitatively characterize the geometric changes between S_0 and S_1 states, the root of the mean of squared displacement $\left(\mathrm{RMSD},\ \mathrm{RMSD} = \sqrt{\frac{1}{N}\sum_{i}^{natom}\left[(x_i - x_i')^2+(y_i - y_i')^2+(z_i - z_i')^2\right]}\right)$ is calculated using VMD software.[47] The larger the RMSD values, the more obvious the geometric changes between S_0 and S_1 states. The calculated RMSDs of investigated molecules are collected in Table 1, and the diagram of structure changes is shown in Fig. S2 in the ESI.† It can be found that the introduction of OBN, BN and BAM units into the *para*-PhCN-based molecular framework causes obviously larger RMSD values compared with the values obtained by introducing them into *meta*-PhCN-based and PhCN-free molecules, which is consistent with the changing trend of $\Delta\theta$ values and can be attributed dominantly to the steric hindrance effects. Nevertheless, the incorporation of CAI and PhCAI units into the *para*-PhCN-based molecular skeleton shows small RMSD values, which can be explained by their relatively weak electronic interactions between adjacent groups upon excitation, originating from the non-HOMO electron distributions of the introduction points. The small RMSD values between S_0 and S_1 states probably lead to favorable non-radiative energy consumption. Therefore, fine modification of the introduction mode and chiral units in

molecules could effectively reduce the non-radiative loss upon excitation.

3.2 Electronic structure–property analyses

Frontier molecular orbitals (FMOs), especially the highest occupied molecular orbital (HOMO) and the lowest unoccupied molecular orbital (LUMO), play important roles in relevant photophysical processes. Herein, the HOMO and LUMO energy levels, gaps, and electronic density distributions were analysed to reveal the electronic properties of the investigated molecules (Fig. 2). The model molecules without introducing chiral units (Fig. S3, ESI,† denoted as *p*-BN, *m*-BN and BN) were studied as a reference. Compared with the corresponding model molecules, the investigated molecules have higher HOMO and LUMO levels because of the introduced electron-donating chiral units. The *para*-PhCN-based molecules exhibit increased LUMO levels (0.06–0.30 eV) more significant than HOMO levels (0.01–0.24 eV), while *meta*-PhCN-based molecules present a more obvious increase in HOMO levels (0.03–0.34 eV) than LUMO levels (0.01–0.19 eV). This situation can be explained by the fact that the *para*- and *meta*-carbon positions of the B-substituted phenyl ring in the MR core correspond to the LUMO and HOMO electron distributions, respectively, which lead to important influences on the corresponding energy levels. For the PhCN-free molecules, the increase in HOMO levels is larger than that in LUMO levels, especially for the ones with relatively stronger electron-donating chiral units (BAM, CAI and PhCAI), resulting in the reduced HOMO–LUMO gaps and thus spectral absorption/emission in the long wavelength range.

The HOMO and LUMO of the investigated molecules are mainly distributed on the atoms with opposite electronic characteristics, which greatly weakens the bonding and anti-bonding properties between adjacent atoms. Such a typical alternate electron distribution of MR materials is beneficial for realizing narrowband emissions. More interestingly, the chiral units of BAM, CAI and PhCAI are prone to participating in the HOMO distributions of *meta*-PhCN- based and PhCN-free molecules, maybe due to the HOMO tending to distribute on the *meta*-carbon position of the B-substituted phenyl ring in the MR core and the gradually increased electron-donating abilities of these chiral units, and we speculate that the chiral units participating in the FMO of molecules would make more obvious perturbation of the CPL signals and thus be beneficial to increase the g_{EL} value.

3.3 Photophysical property investigations

The absorption and emission properties play important roles in the performance of TADF materials, and an ideal emitter should exhibit effective energy utilization and outstanding color purity. As discussed above, the introduction modes and the electron-donating ability of chiral units have a distinct influence on the geometric and electronic structures, which

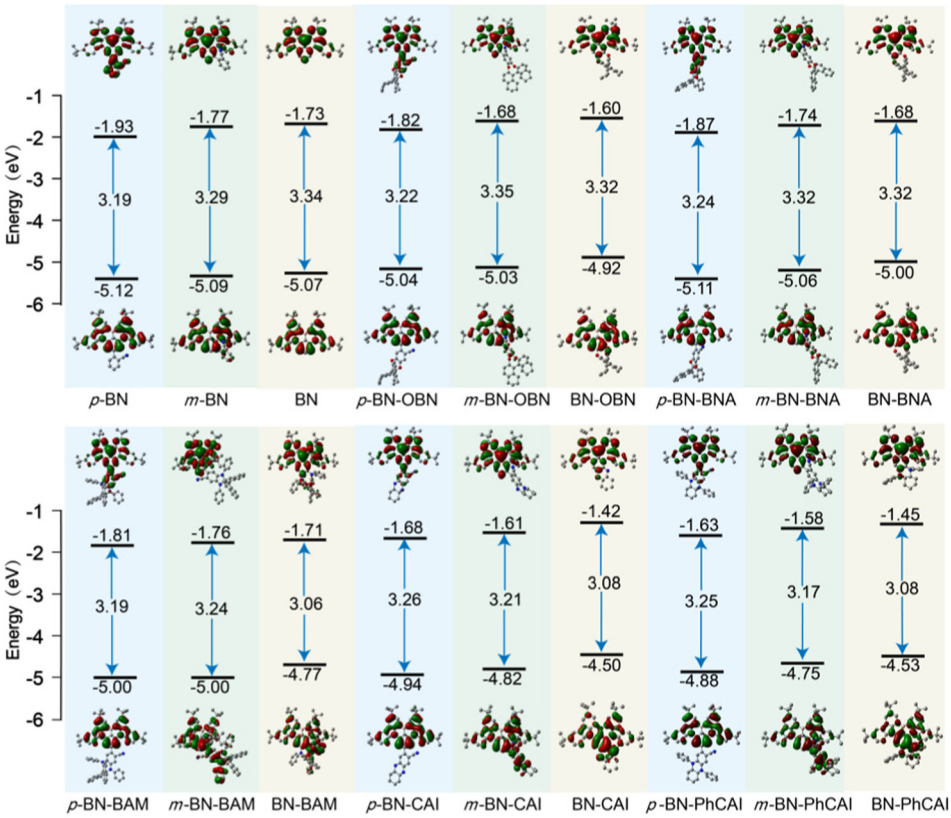

Fig. 2 Frontier orbital electronic density distributions, energy levels, and HOMO–LUMO gaps of the designed molecules and corresponding model molecules.

should also affect the absorption and emission properties of the studied molecules. The simulated emission spectra of the investigated molecules are shown in Fig. 3. The maximum absorption and emission wavelengths (λ_{abs} and λ_{PL}), transition characters and FWHM values (emission bands at long wavelength) are collected in Table S2 (ESI†). The simulated λ_{PL} of the experimental molecule *p*-BN-OBN is 488 nm, fitting the experimental result (λ_{PL} = 493 nm) well, which further verifies the reliability of the selected calculation method. Compared with the model molecules *p*-BN, *m*-BN and BN, the corresponding molecules with the introduced chiral units basically show blue-shifted, red-shifted and red-shifted λ_{abs} (λ_{PL}), respectively, which are consistent with the changing trend of their HOMO–LUMO gaps. For the *meta*-PhCN-based and PhCN-free molecules, the introduction of BAM, CAI, and PhCAI groups could significantly red-shift λ_{abs} and λ_{PL} owing to the relatively stronger electron-donating abilities of the chiral units and their enhanced interactions with the BN core, which provides a possible molecular design strategy for constructing orange and red CP-TADF materials.

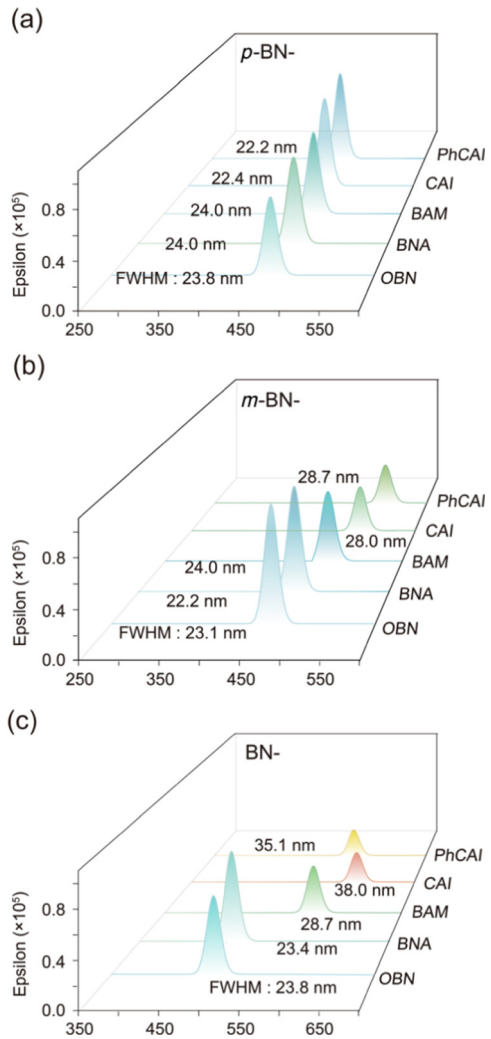

Fig. 3 Simulated emission spectra of (a) *para*-PhCN-based, (b) *meta*-PhCN-based, and (c) PhCN-free series molecules with FWHM in unit of nm.

The absorption and emission bands in the lowest energy region mainly originate from the transition from the HOMO to the LUMO, that is, the short-range charge transfer transition from the electron-donating N atoms to the electron-deficient B atoms. Such characteristics can also be seen from the analysis of the charge density difference between the single excited state and the ground state (Fig. S4, ESI†), which is beneficial for obtaining narrowband emission. Because of the scale inversion, the same peak may appear narrower or broader (smaller or larger FWHM values in unit of nm) depending on the absolute emission peak position. Therefore, both the units of nm and eV are taken into account to make comparisons, and the simulated FWHM values are indicated in Fig. 3 and Table S2 (ESI†). The emission spectral FWHM of the experimental molecule *p*-BN-OBN is 24 nm/0.12 eV calculated by means of Gaussian functions with the spectral broadening setting of 500 cm^{-1}, which is in good agreement with the experimental result (FWHM = 22 nm in toluene). Such a setting method has been widely used for the emission spectral predictions and comparisons of MR-materials.[39,48,49] For the *para*-PhCN-based molecules, the introduction of chiral units with different electron-donating capabilities has little impact on emission spectral FWHM, while the introduction of chiral units with relatively stronger electron-donating abilities, such as BAM, CAI and PhCAI, the FWHM increased by 2–6 nm and 5–15 nm for the *meta*-PhCN-based and PhCN-free molecules, respectively; the enhanced intramolecular charge transfer characteristics reduce the narrowband emission properties of the materials, which is consistent with the conventional effects of charge transfer on emission.[50] In comparison with *p*-BN-OBN, most of the investigated molecules exhibit slightly broader or comparable emission spectra, but possess FWHMs still within 0.14 eV, maintaining the narrowband emission properties.[51]

In principle, the width of the emission spectra is closely related to the reorganization energy (λ) between the ground and excited states. The rigid BN featuring multiple-resonance properties weakens the bonding and anti-bonding properties between adjacent atoms upon excitation, and decreases the vibration coupling between adjacent vibration levels observed from the small Huang–Rhys factor in the low-frequency region (Fig. S5, ESI†), contributing to the small reorganization energy (0.07 eV, the calculation details are shown in Fig. S6, ESI†) and extremely narrowband emission.[19,40,52] Such molecular characters can still be clearly seen in the *p*-BN-OBN and the design molecules (Fig. 2 and Fig. S5, ESI†), and the designed molecules possess relatively small or comparable reorganization energies (0.06–0.39 eV, Table S2, ESI†) compared with the experimental molecule *p*-BN-OBN (λ = 0.33 eV, FWHM 22 nm in experiment), even though larger than that of BN, basically maintaining the narrowband emission. We speculate that the increased λ observed in the investigated molecules results from the molecular relaxation of chiral units, but the involvement of chiral units in the electronic transition is limited.

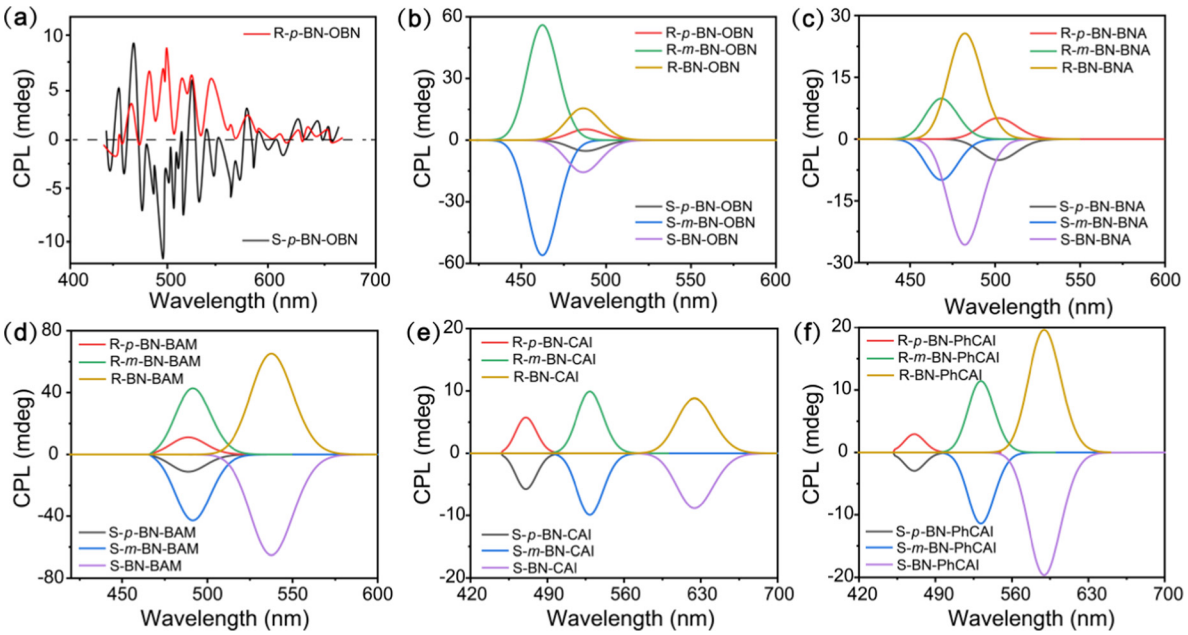

Fig. 4 Experimental CPL spectrum of (a) *p*-BN-OBN and simulated CPL spectra of (b) OBN, (c) BNA, (d) BAM, (e) CAI and (f) PhCAI series molecules.

3.4 Chiral property investigations

The chiral properties of the molecules were investigated using the electronic circular dichroism (ECD) and circular polarization luminescence (CPL) spectra based on the optimized ground state and excited state, respectively. The degree of circular polarization is quantified by the dissymmetry factor, *i.e.*, the relative intensity difference of the left and right circularly polarized absorption (g_{abs} in ECD) or emission (g_{PL} in CPL), respectively, which can be theoretically estimated according to the following equation:

$$g = \frac{4|\mu||m|\cos\theta}{|\mu|^2 + |m|^2} \cong \frac{4|m|\cos\theta}{|\mu|}$$

where μ and m represent the transition electric dipole moment and transition magnetic dipole moment, respectively, and θ is the angle between them. Due to a much smaller value of $|m|$ in comparison with that of $|\mu|$, $|m|^2$ can be omitted. Consequently, g is inversely proportional to the amplitude of μ and directly proportional to m, as well as cosine of their relative angle (θ). Nevertheless, the transition with a small $|\mu|$ generally leads to a low fluorescence quantum yield, which is proportional to $|\mu|^2$. Therefore, CPL materials simultaneously exhibiting a large g_{PL} value and high fluorescence quantum yield is desired and challenging to achieve.

The ECD (Fig. S7, ESI†) and CPL (Fig. 4) spectra of the investigated molecules are simulated, and the detailed parameters are collected in Table 2. As illustrated in Fig. S7 (ESI†), each pair of enantiomers of the investigated molecules show symmetric ECD spectra with opposite Cotton effects in the lowest energy region, indicating the successful chirality transfer from the chiral perturbation units into the MR skeletons. Similarity, each pair of enantiomers (Fig. 4) exhibit mirror-image CPL spectra mainly stemming from the $S_1 \rightarrow S_0$ transition, further manifesting the chirality transfer features of

Table 2 Calculated key parameters related to g_{PL} of CPL

Compd.	$\|\mu\|$ ($\times 10^{-18}$ esu cm)	$\|m\|$ ($\times 10^{-20}$ erg G^{-1})	$\|m\|/\|\mu\|$	$\theta_{\mu,m}$ (°)	r_c (Å)	g_{PL}
p-BN-OBN	6.31	2.15	0.34	89.6	10.21	9.16×10^{-5}
m-BN-OBN	6.22	2.28	0.37	84.9	9.82	1.30×10^{-3}
BN-OBN	5.98	1.24	0.21	86.9	7.44	4.50×10^{-4}
p-BN-BNA	6.17	1.90	0.31	89.7	10.11	7.10×10^{-5}
m-BN-BNA	6.60	1.89	0.29	89.0	9.70	1.95×10^{-4}
BN-BNA	6.00	1.11	0.19	84.6	7.45	6.98×10^{-4}
p-BN-BAM	5.95	2.64	0.44	89.3	9.98	2.27×10^{-4}
m-BN-BAM	5.05	1.82	0.36	83.9	8.69	1.53×10^{-3}
BN-BAM	4.83	0.99	0.20	70.9	6.95	2.69×10^{-3}
p-BN-CAI	6.67	1.12	0.17	89.0	8.71	1.17×10^{-4}
m-BN-CAI	4.49	0.77	0.17	86.4	7.90	4.25×10^{-4}
BN-CAI	4.42	0.54	0.12	82.3	6.73	6.59×10^{-4}
p-BN-PhCAI	6.54	2.18	0.33	89.7	8.87	6.51×10^{-5}
m-BN-PhCAI	4.19	1.22	0.29	87.4	8.25	5.34×10^{-4}
BN-PhCAI	4.26	0.85	0.20	81.0	5.70	1.25×10^{-3}

the S_1 states. The calculated g_{PL} value of *p*-BN-OBN is 9.16 × 10^{-5}, which is underestimated compared with its experimental value of 9.0 × 10^{-4}; the actual *g* values of the new designed materials should be even higher. For the molecules with the same chiral units, the *para*-PhCN-based molecules show g_{PL} on the order of 10^{-5}–10^{-4}, while *meta*-PhCN-based and PhCN-free molecules exhibit gradually increased g_{PL} values (10^{-4}–10^{-3}) mainly owing to the favorable adjustment of the angle (θ) between the transition electric dipole moment and the transition magnetic dipole moment, the more the θ away from the 90°, the larger the g_{PL} values (Fig. 5). Specifically, the centroid distance (r_c) between the MR core and the chiral unit is calculated and is shown in Table 2, and it can be found that the r_c shows a decreasing trend from *para*-PhCN-based, *meta*-PhCN-based to PhCN-free molecules. In other words, the closer the chiral unit is to the MR core, the more effective the chiral unit perturbs the MR core, which provides a possible molecular design strategy to construct materials with high *g* values. Moreover, the relatively stronger electron-donating chiral units of BAM, CAI and PhCAI participate in the HOMO distributions of the corresponding *meta*-PhCN-based and PhCN-free molecules, which indeed leads to relatively obvious ECD and CPL signals, and the more the chiral unit participation in the HOMO composition, basically the larger the g_{PL} value (Fig. S8 and Table S3, ESI†), but inevitably reduced $|\mu|$ because of the increased intramolecular charge transfer. Therefore, both the chiral perturbation units and their introduction mode should be considered to modulate the CP-TADF properties of the materials, and the materials incorporating a moderate electron-donating chiral unit (BAM) closer to the chromophore of molecular skeleton may achieve a balance between the contradictory requirements of a large *g* value and high fluorescence quantum yield.

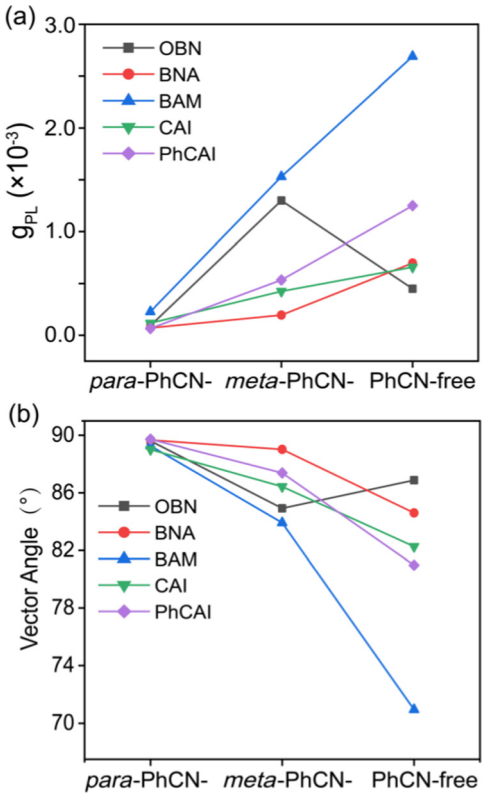

Fig. 5 Calculated (a) g_{PL} values and (b) vector angles of the molecules with different chiral units and introduction modes.

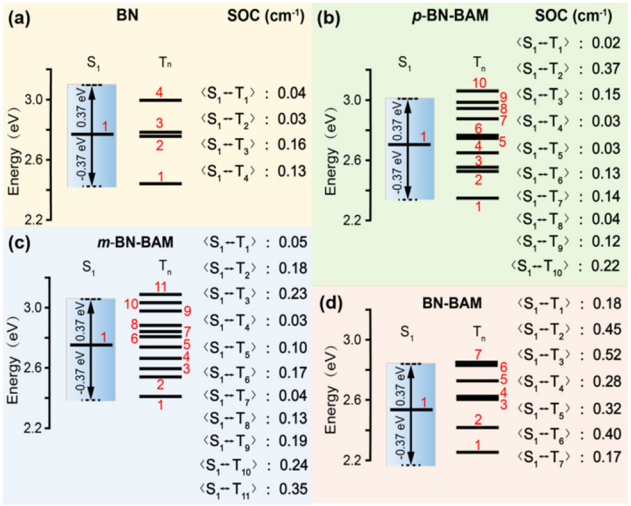

Fig. 6 Calculated vertical excitation energies and the SOC constants between S_1 and T_n states for (a) BN, (b) *p*-BN-BAM, (c) *m*-BN-BAM and (d) BN-BAM in toluene.

3.5 TADF property analyses

An efficient RISC process and high fluorescence quantum yield are of vital significance for high-performance TADF materials. Herein, we analyzed the properties related to RISC and radiative decay processes of the investigated molecules briefly. According to the energy gap law, the minimization of the energy gap between the singlet and triplet excited states is the minimum requirement to promote the RISC process. Based on the vertical singlet and triplet excitation energies calculated with TD-DFT methods, there are 3–11 channels exhibiting an energy gap below 0.37 eV between the S_1 and triplet states for the investigated molecules, as shown in Fig. 6 and Fig. S9 (ESI†). Meanwhile, following the El-Sayed's rule, some possible RISC channels are further supported by the large SOC values higher than 0.1 cm^{-1} due to the intrinsic n–π transition favored by the heteroatom involvement in the designed molecules.[53,54] Specifically, the molecules with the BAM chiral unit show an increased number of channels having large SOC values compared with BN, a typical MR-TADF material, which are important to realize efficient RISC process. Furthermore, the fluorescence rate (k_r, radiative decay from S_1 to S_0 state) is calculated using the MOMAP program, together with the oscillator strength (*f*) obtained from TD-DFT calculations, as shown in Table S4 (ESI†). The molecules having small *f* values basically show small k_r as expected, and the *meta*-PhCN-based and PhCN-free molecules with the BAM chiral unit show relatively high performance taking both the g_{PL} and k_r values into

account, which is in agreement with the above discussion. Considering the fact that k_r is strongly affected by the experimental factors, such as solvent polarity, temperature, solution pH values, and so on, the calculated k_r can be regarded as a reference.

4. Conclusions

In this work, we present a systematic theoretical investigation on the CP-MR-TADF materials with different introduction modes of peripheral groups and types of chiral perturbation units designed using an updated chiral perturbation strategy, aiming to elucidate the structure–property relationship and construct high-performance CP-MR-TADF materials. From the analyses of the geometric and electronic structures, the photophysical and chiral properties, and the parameters related to TADF properties, we found that (1) the designed molecules with the introduction of chiral perturbation units maintain the alternating LUMO and HOMO distributions on B and N atoms, and short-range charge transfer transition upon excitation, which is of benefit to achieve narrowband emission; (2) the *meta*-PhCN-based and PhCN-free molecules possessing small centroid distances between the chiral unit and the B/N skeleton show large simulated g_{PL} values, possibly owing to a large degree of chiral perturbation of the CPL signals; (3) the relatively stronger electron-donating chiral units of BAM, CAI and PhCAI participate in the HOMO distributions of the corresponding *meta*-PhCN-based and PhCN-free molecules, which is favorable for obtaining large g values but inevitably reduced $|\mu|$ and thus florescence rate because of the increased intramolecular charge transfer and decreased HOMO–LUMO overlap; and (4) the molecules with the BAM chiral unit show an increased number of RISC channels with large SOC values compared to the typical MR-TADF material of BN, which are important to realize efficient RISC process and thus desired TADF properties. In all, the participatory chiral perturbation, where the chiral perturbation unit is close to the chromophores and participating in the frontier molecular orbital distributions, is promising to realize a large degree of chiral perturbation, providing important clues for the design and construction of high-performance CP-MR-TADF materials.

Author contributions

Ping Li and Wenjing Li carried out theoretical calculations and wrote the draft of the manuscript; Qixin Lv discussed the molecular design and analysis; and Runfeng Chen and Chao Zheng provided guidance on calculations, discussed the results and edited the manuscript.

Conflicts of interest

There are no conflicts to declare.

Acknowledgements

The authors acknowledge the financial support from the National Natural Science Foundation of China (22275097, 61875090, 21772095, and 91833306), Key giant project of Jiangsu Educational Committee (19KJA180005), the fifth 333 project of Jiangsu Province of China (BRA2019080), 1311 Talents Program of Nanjing University of Posts and Telecommunications, Natural Science Foundation of Jiangsu Higher Education Institutions (22KJB150030), Scientific Starting Fund from Nanjing University of Posts and Telecommunications (NUPTSF) (NY219160), and Nature Science Foundation of Nanjing University of Posts and Telecommunications (NY221092, NY222148).

Notes and references

1 L. Frédéric, A. Desmarchelier, L. Favereau and G. Pieters, *Adv. Funct. Mater.*, 2021, **31**, 2010281.
2 Y. Sang, J. Han, T. Zhao, P. Duan and M. Liu, *Adv. Mater.*, 2020, **32**, 1900110.
3 J. Han, S. Guo, H. Lu, S. Liu, Q. Zhao and W. Huang, *Adv. Opt. Mater.*, 2018, **6**, 1800538.
4 J. R. Brandt, F. Salerno and M. J. Fuchter, *Nat. Rev. Chem.*, 2017, **1**, 0045.
5 Y. Wang, D. Niu, G. Ouyang and M. Liu, *Nat. Commun.*, 2022, **13**, 1710.
6 Y. Zhang, H. Li, Z. Geng, W. Zheng, Y. Quan and Y. Cheng, *Nat. Commun.*, 2022, **13**, 4905.
7 F.-C. Kong, S.-Y. Yang, X.-J. Liao, Z.-Q. Feng, W.-S. Shen, Z.-Q. Jiang, D.-Y. Zhou, Y.-X. Zheng and L.-S. Liao, *Adv. Funct. Mater.*, 2022, **32**, 2201512.
8 Y.-P. Zhang, M.-X. Mao, S.-Q. Song, Y. Wang, Y.-X. Zheng, J.-L. Zuo and Y. Pan, *Angew. Chem., Int. Ed.*, 2022, **61**, e202200290.
9 X. Gao, J. Wang, K. Yang, B. Zhao and J. Deng, *Chem. Mater.*, 2022, **34**, 6116–6128.
10 Y.-P. Zhang, X. Liang, X.-F. Luo, S.-Q. Song, S. Li, Y. Wang, Z.-P. Mao, W.-Y. Xu, Y.-X. Zheng, J.-L. Zuo and Y. Pan, *Angew. Chem., Int. Ed.*, 2021, **60**, 8435–8440.
11 Y.-X. Yuan, J.-H. Jia, Y.-P. Song, F.-Y. Ye, Y.-S. Zheng and S.-Q. Zang, *J. Am. Chem. Soc.*, 2022, **144**, 5389–5399.
12 T. Hatakeyama, K. Shiren, K. Nakajima, S. Nomura, S. Nakatsuka, K. Kinoshita, J. Ni, Y. Ono and T. Ikuta, *Adv. Mater.*, 2016, **28**, 2777–2781.
13 Y. Kondo, K. Yoshiura, S. Kitera, H. Nishi, S. Oda, H. Gotoh, Y. Sasada, M. Yanai and T. Hatakeyama, *Nat. Photonics*, 2019, **13**, 678–682.
14 S. Oda, B. Kawakami, R. Kawasumi, R. Okita and T. Hatakeyama, *Org. Lett.*, 2019, **21**, 9311–9314.
15 J. Han, Z. Huang, X. Lv, J. Miao, Y. Qiu, X. Cao and C. Yang, *Adv. Opt. Mater.*, 2022, **10**, 2102092.
16 Y. X. Hu, J. Miao, T. Hua, Z. Huang, Y. Qi, Y. Zou, Y. Qiu, H. Xia, H. Liu, X. Cao and C. Yang, *Nat. Photonics*, 2022, **16**, 803–810.
17 Y. Xu, C. Li, Z. Li, Q. Wang, X. Cai, J. Wei and Y. Wang, *Angew. Chem., Int. Ed.*, 2020, **59**, 17442–17446.

18 S.-N. Zou, C.-C. Peng, S.-Y. Yang, Y.-K. Qu, Y.-J. Yu, X. Chen, Z.-Q. Jiang and L.-S. Liao, *Org. Lett.*, 2021, **23**, 958–962.
19 X. Qiu, G. Tian, C. Lin, Y. Pan, X. Ye, B. Wang, D. Ma, D. Hu, Y. Luo and Y. Ma, *Adv. Opt. Mater.*, 2021, **9**, 2001845.
20 Y. Xu, Q. Wang, X. Cai, C. Li and Y. Wang, *Adv. Mater.*, 2021, **33**, 2100652.
21 X. Wu, J.-W. Huang, B.-K. Su, S. Wang, L. Yuan, W.-Q. Zheng, H. Zhang, Y.-X. Zheng, W. Zhu and P.-T. Chou, *Adv. Mater.*, 2022, **34**, 2105080.
22 J.-K. Li, X.-Y. Chen, Y.-L. Guo, X.-C. Wang, A. C. H. Sue, X.-Y. Cao and X.-Y. Wang, *J. Am. Chem. Soc.*, 2021, **143**, 17958–17963.
23 W. Yang, N. Li, J. Miao, L. Zhan, S. Gong, Z. Huang and C. Yang, *CCS Chem.*, 2022, **4**, 3463–3471.
24 S.-Y. Yang, S.-N. Zou, F.-C. Kong, X.-J. Liao, Y.-K. Qu, Z.-Q. Feng, Y.-X. Zheng, Z.-Q. Jiang and L.-S. Liao, *Chem. Commun.*, 2021, **57**, 11041–11044.
25 J. M. dos Santos, D. Sun, J. M. Moreno-Naranjo, D. Hall, F. Zinna, S. T. J. Ryan, W. Shi, T. Matulaitis, D. B. Cordes, A. M. Z. Slawin, D. Beljonne, S. L. Warriner, Y. Olivier, M. J. Fuchter and E. Zysman-Colman, *J. Mater. Chem. C*, 2022, **10**, 4861–4870.
26 Y. Yang, N. Li, J. Miao, X. Cao, A. Ying, K. Pan, X. Lv, F. Ni, Z. Huang, S. Gong and C. Yang, *Angew. Chem., Int. Ed.*, 2022, **61**, e202202227.
27 X.-J. Liao, D. Pu, L. Yuan, J. Tong, S. Xing, Z.-L. Tu, J.-L. Zuo, W.-H. Zheng and Y.-X. Zheng, *Angew. Chem., Int. Ed.*, 2023, **62**, e202217045.
28 K. Senthilkumar, M. Kondratowicz, T. Lis, P. J. Chmielewski, J. Cybińska, J. L. Zafra, J. Casado, T. Vives, J. Crassous, L. Favereau and M. Stępień, *J. Am. Chem. Soc.*, 2019, **141**, 7421–7427.
29 A. Robert, G. Naulet, H. Bock, N. Vanthuyne, M. Jean, M. Giorgi, Y. Carissan, C. Aroulanda, A. Scalabre, E. Pouget, F. Durola and Y. Coquerel, *Chem. – Eur. J.*, 2019, **25**, 14364–14369.
30 F.-M. Xie, J.-X. Zhou, X.-Y. Zeng, Z.-D. An, Y.-Q. Li, D.-X. Han, P.-F. Duan, Z.-G. Wu, Y.-X. Zheng and J.-X. Tang, *Adv. Opt. Mater.*, 2021, **9**, 2100017.
31 M. Li, S.-H. Li, D. Zhang, M. Cai, L. Duan, M.-K. Fung and C.-F. Chen, *Angew. Chem., Int. Ed.*, 2018, **57**, 2889–2893.
32 S. Feuillastre, M. Pauton, L. Gao, A. Desmarchelier, A. J. Riives, D. Prim, D. Tondelier, B. Geffroy, G. Muller, G. Clavier and G. Pieters, *J. Am. Chem. Soc.*, 2016, **138**, 3990–3993.
33 S. Sun, J. Wang, L. Chen, R. Chen, J. Jin, C. Chen, S. Chen, G. Xie, C. Zheng and W. Huang, *J. Mater. Chem. C*, 2019, **7**, 14511–14516.
34 Y. Liu, X. Xiao, Y. Ran, Z. Bin and J. You, *Chem. Sci.*, 2021, **12**, 9408–9412.
35 M. Yang, S. Shikita, H. Min, I. S. Park, H. Shibata, N. Amanokura and T. Yasuda, *Angew. Chem., Int. Ed.*, 2021, **60**, 23142–23147.
36 Y. Zhang, D. Zhang, T. Huang, A. J. Gillett, Y. Liu, D. Hu, L. Cui, Z. Bin, G. Li, J. Wei and L. Duan, *Angew. Chem., Int. Ed.*, 2021, **60**, 20498–20503.
37 X. Liang, Z.-P. Yan, H.-B. Han, Z.-G. Wu, Y.-X. Zheng, H. Meng, J.-L. Zuo and W. Huang, *Angew. Chem., Int. Ed.*, 2018, **57**, 11316–11320.
38 Y. Zhang, D. Zhang, J. Wei, Z. Liu, Y. Lu and L. Duan, *Angew. Chem., Int. Ed.*, 2019, **58**, 16912–16917.
39 Y. Zhang, D. Zhang, J. Wei, X. Hong, Y. Lu, D. Hu, G. Li, Z. Liu, Y. Chen and L. Duan, *Angew. Chem., Int. Ed.*, 2020, **59**, 17499–17503.
40 Y. Xu, Z. Cheng, Z. Li, B. Liang, J. Wang, J. Wei, Z. Zhang and Y. Wang, *Adv. Opt. Mater.*, 2020, **8**, 1902142.
41 P. Jiang, L. Zhan, X. Cao, X. Lv, S. Gong, Z. Chen, C. Zhou, Z. Huang, F. Ni, Y. Zou and C. Yang, *Adv. Opt. Mater.*, 2021, **9**, 2100825.
42 J.-z Fan, S. Qiu, L.-l Lin and C.-k Wang, *Chin. J. Chem. Phys.*, 2016, **29**, 291–296.
43 T. Lu and F. Chen, *J. Comput. Chem.*, 2012, **33**, 580–592.
44 F. Neese, *Wiley Interdiscip. Rev.: Comput. Mol. Sci.*, 2022, **12**, e1606.
45 Z. Shuai, *Chin. J. Chem.*, 2020, **38**, 1223–1232.
46 Z. Shuai and Q. Peng, *Natl. Sci. Rev.*, 2017, **4**, 224–239.
47 W. Humphrey, A. Dalke and K. Schulten, *J. Mol. Graphics*, 1996, **14**, 33–38.
48 Y. Zhang, J. Wei, D. Zhang, C. Yin, G. Li, Z. Liu, X. Jia, J. Qiao and L. Duan, *Angew. Chem., Int. Ed.*, 2022, **61**, e202113206.
49 S. Lin, Q. Ou and Z. Shuai, *ACS Mater. Lett.*, 2022, **4**, 487–496.
50 X.-C. Fan, K. Wang, Y.-Z. Shi, J.-X. Chen, F. Huang, H. Wang, Y.-N. Hu, Y. Tsuchiya, X.-M. Ou, J. Yu, C. Adachi and X.-H. Zhang, *Adv. Opt. Mater.*, 2022, **10**, 2101789.
51 F. Liu, Z. Cheng, L. Wan, Z. Feng, H. Liu, H. Jin, L. Gao, P. Lu and W. Yang, *Small*, 2022, **18**, 2106462.
52 X. Ye, L. Xu, F. Qiu, Z. Ma, B. Wang, J. Zhou, S. Xiong, Y. Ma, D. Hu and G. Tian, *Energy Fuels*, 2021, **35**, 19139–19145.
53 J. Li, F. Zhao, Y. Chen, M. Zhang, T. Li and H. Zhang, *J. Mater. Chem. C*, 2021, **9**, 15309–15320.
54 Y. Song, B. Li, S. Liu, M. Qin, Y. Gao, K. Zhang, L. Lin, C.-K. Wang and J. Fan, *J. Mater. Chem. C*, 2022, **10**, 4723–4736.